Research Article | Vol. 30, No. 10 / 9 May 2022 / Optics Express 17321
Optics EXPRESS

Flip-component metasurfaces for camouflaged meta-domes

HONGCHEN CHU,[1] YE ZHANG,[1] XIAOXUAN MA,[1] XIANG XIONG,[1] RUWEN PENG,[1,3] MU WANG,[1,2,4] AND YUN LAI[1,5]

[1]National Laboratory of Solid State Microstructures, School of Physics, and Collaborative Innovation Center of Advanced Microstructures, Nanjing University, Nanjing 210093, China
[2]American Physical Society, 1 Research Road, Ridge, NY 11961, USA
[3]rwpeng@nju.edu.cn
[4]muwang@nju.edu.cn
[5]laiyun@nju.edu.cn

Abstract: Allowing microwaves to transmit through without changing the wavefront is one of the essential requirements of the dome structures of antenna arrays like radars. Here, we demonstrate a microwave metasurface as an array of two types of meta-atoms, which are the flip counterparts to each other. Due to the reciprocity and space-inversion symmetry, the wavefront in the transmission is unchanged by the metasurface in a broad spectrum; while at the same time, the wavefront in reflection can be manipulated independently by changing the arrangement of the meta-atoms. Specifically, a random-flip metasurface that produces diffuse reflection is realized, enabling a camouflaged meta-dome. The broadband, wide-angle, and polarization-independent diffuse reflection and undistorted transmission are numerically and experimentally verified. Our finding enables a unique meta-dome structure that has camouflage functionality.

1. Introduction

In the past decades, as the two-dimensional (2D) counterpart of the bulky metamaterial [1,2], metasurfaces [3,4] composed of subwavelength meta-atoms have shown tremendous power in manipulating the intensity, wavefront, and polarization of electromagnetic waves, which aroused great interest. To date, metasurfaces have been successfully employed in many intriguing applications, including anomalous reflection and refraction [5–8], metalens [9–12], propagating-to-evanescent wave conversion [13–17], high-efficiency holograms, and colorful holograms [18–21], ultrathin invisibility cloaks [22–26], antireflection coatings [26–29], structured light generation [30–32] and polarization states converter [33–37], etc.

For most of the metasurfaces that allow both transmission and reflection, manipulated transmission and manipulated reflection always appear in pairs [5,6,38–41], as schematically shown in Fig. 1(a). This phenomenon usually applies to both the metasurfaces with resonant phase shift [5–7] and geometric phase shift, i.e., Pancharatnam-Berry (PB) phase [38–42]. The correlation between the manipulated reflection and transmission is understandable from the properties of the interaction between light and meta-atoms. A resonance in the meta-atom usually influences both the reflection and transmission. While for PB-phase-based metasurface, the phase shifts of a PB meta-atom in transmission and reflection are equal [40,41]. Hence, the wavefronts of both reflection and transmission are usually modified at the same time, leading to the simultaneous existence of manipulated transmission and manipulated reflection.

However, in practice, there are many scenarios where only manipulated reflection is required. The wavefront in transmission, on the contrary, is often preferred not to be influenced by the metasurface, such that the information carried by the incident waves can be well conserved and received by the device behind the metasurface. One typical case is the requirement of

#456655 https://doi.org/10.1364/OE.456655
Journal © 2022 Received 18 Feb 2022; revised 21 Apr 2022; accepted 25 Apr 2022; published 4 May 2022

Optics EXPRESS

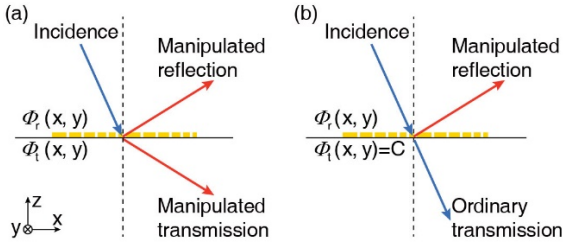

Fig. 1. Schematic diagram of the flip-component metasurface that controls reflection independently. (a) Metasurface induces simultaneously manipulated reflection and manipulated transmission. (b) The flip-component metasurface produces manipulated reflection and ordinary transmission simultaneously.

transparency in optical systems, which demands that the wavefront of the transmitted light can form a virtual image of the object. Very recently, a random-flip metasurface that realizes the coalescence of diffuse reflection and undistorted transmission is demonstrated in the infrared and visible frequency regime [43]. Such an intriguing phenomenon can eliminate the reflective image and glare without sacrificing the transparency. Another important case is the dome structure of antenna arrays like radars, which keeps the incident wavefront unchanged in transmission for broadband microwave. On the other hand, configurable reflection is desired because it bestows the precious functionality of camouflage. However, to date, such a dome structure that enables camouflage has not been reported yet.

In this work, we demonstrate an ultrathin and freestanding microwave metasurface, which supports ordinary transmission with unchanged wavefront and configurable reflection at the same time. The metasurface is composed of two types of meta-atoms (components), which are the flipped counterparts to each other. Such meta-atoms have exactly the same transmittance and transmission phase under the protection of the reciprocity and space-inversion symmetry. Therefore, the wavefront in the transmission is unchanged no matter what the arrangement of the meta-atoms is. The reflection, on the contrary, can be independently manipulated by altering the arrangement of the meta-atoms. As an example, we designed a metasurface that supports diffuse reflection and undistorted transmission in a broad microwave spectrum for arbitrary polarization. This remarkable property enables the realization of camouflaged meta-domes. The polarization-independent and broadband performance of the metasurface is verified by numerical simulations and both near-field and far-field measurements. Our work opens a metasurface route towards camouflaged meta-domes.

2. Principle of independently manipulated reflection

To achieve the independently manipulated reflection and ordinary transmission simultaneously, as schematically shown in Fig. 1(b), the phase shift distributions $\Phi_r(x, y)$ should be introduced to the reflection without affecting the constant phase shift distributions of the transmission, i.e. $\Phi_t(x, y) = C$. These two requirements can be simultaneously achieved by arranging two types of meta-atoms with distinctly different reflection and identical transmission. To achieve this goal, we consider a pair of meta-atoms, which are asymmetric in the normal direction and are the flip counterparts to each other. In analogy with the two sides of a coin (heads and tails), such two types of meta-atoms are referred to as "heads meta-atom" (HMA) and "tails meta-atom" (TMA). The transmission and reflection coefficients of the HMA are t and r, respectively, as schematically shown in case I in Fig. 2(a). The reciprocity theorem ensures that when the incidence channel and the transmission channel are exchanged (case II in Fig. 2(a)), the transmission coefficient remains unchanged, i.e., $t = t'$. By carrying out space-inversion (flip) operation on case II, case

Optics EXPRESS

III in Fig. 2(a) is obtained, where both the reflection and transmission coefficients are equal to those of case II, i.e., $t' = t''$ and $r' = r''$. At the same time, the HMA (TMA) changes into the flip counterpart, i.e. the TMA (HMA) in case I. Here, we note that to avoid the complication of polarization change, the HMA and TMA are both designed to be symmetric in the x and y-directions. By comparing case I and case III, it is found that HMA and TMA have exactly the same transmission coefficients under any incident angle, i.e. $t = t''$. On the contrary, the reflection coefficients of the HMA and TMA can be distinctly different, i.e., $r \neq r''$. Hence, this is a universal approach to designing two types of meta-atoms with identical transmission and distinctly different reflection.

By using this method, we designed two types of meta-atoms represented in Fig. 2(b) as a proof of concept in the microwave regime. The two types of meta-atoms are the flip counterparts to each other. They are composed of two metallic layers of a Minkowski loop and a square frame separated by a dielectric spacer with a thickness of $h = 2mm$ and a relative permittivity of $\varepsilon_r = 2.65$. The lattice constant of the meta-atoms is $p = 10.2mm$. The other detailed structural parameters of the metallic patterns depicted in Fig. 2(b) are specified in the figure caption. Numerical simulations based on the finite-element method are carried out to investigate the designed meta-atoms. The calculated amplitude and phase in transmission and reflection for the two types of meta-atoms under incidence with both transverse electric (TE) and transverse magnetic (TM) polarizations at the incident angles of 0°, 30° and 60° are shown in Fig. 2(c-f), respectively, where the solid lines depict HMA and symbols depict TMA. From Figs. 2(c) and 2(d), it is seen that the transmission amplitude and phase of HMA and TMA are the same regardless of the incident angle and polarization, which is coincident with the theoretical prediction. Figure 2(e) illustrates that the reflection amplitude of HMA and TMA are also identical, because of the negligible loss in the meta-atoms and the principle of energy conservation. However, the reflection phases of the two types of meta-atoms depicted by φ_r^{HMA} and φ_r^{TMA} are distinctly different, as shown in Fig. 2(f). The reflection phase difference between HMA and TMA under normal incidence reaches the maximum value of 180° at 11.16 GHz. Such a phase difference changes from 160° to 200° within the frequency range from 10.77 GHz to 11.57 GHz, as depicted by the gray shadow. Bandwidth of such phase difference can be further extended by engineering the resonant modes in the meta-atoms by optimizing the geometric parameters of the metallic patterns, the thickness and permittivity of the dielectric spacer, etc. Moreover, since the meta-atoms have C4v symmetry in the x-y plane, the reflection phase differences are the same for both TE and TM polarizations. This phase difference varies slowly with the incident angle within ±60°.

By arranging the two types of meta-atoms shown in Fig. 2(b) to construct a metasurface, the reflection can be engineered by designing the pattern of the meta-atoms to form binary phase distributions of reflection, i.e., $\Phi_r(x, y)$, where x and y represent the location on the metasurface and Φ_r can be either φ_r^{HMA} or φ_r^{TMA}. The transmission of the metasurface is uninfluenced by this arrangement and $\Phi_t(x, y) = C$ is maintained. Binary phase elements have been adopted to realize numerous electromagnetic wave controlling including diffuse reflection and transmission, beam splitting, focusing, vertex beam generation, etc. Therefore, all these functionalities in reflection can be integrated with the ordinary transmission, respectively, in the flip-component metasurface. We also note that for incidence from the other side of the flip-component metasurface, the same transmission phase distribution $\Phi_t'(x, y) = C$ and a complementary reflection phase distribution, i.e., $\Phi_r'(x, y) = -\Phi_r(x, y) + \varphi_r^{HMA} + \varphi_r^{TMA}$ is obtained. Thus the flip-component metasurface with specific functionality works for incidence from both sides. In the following, we utilize a random configuration to combine diffuse reflection and undistorted transmission, which might find application in dome structures for radars, i.e. radomes.

Optics EXPRESS

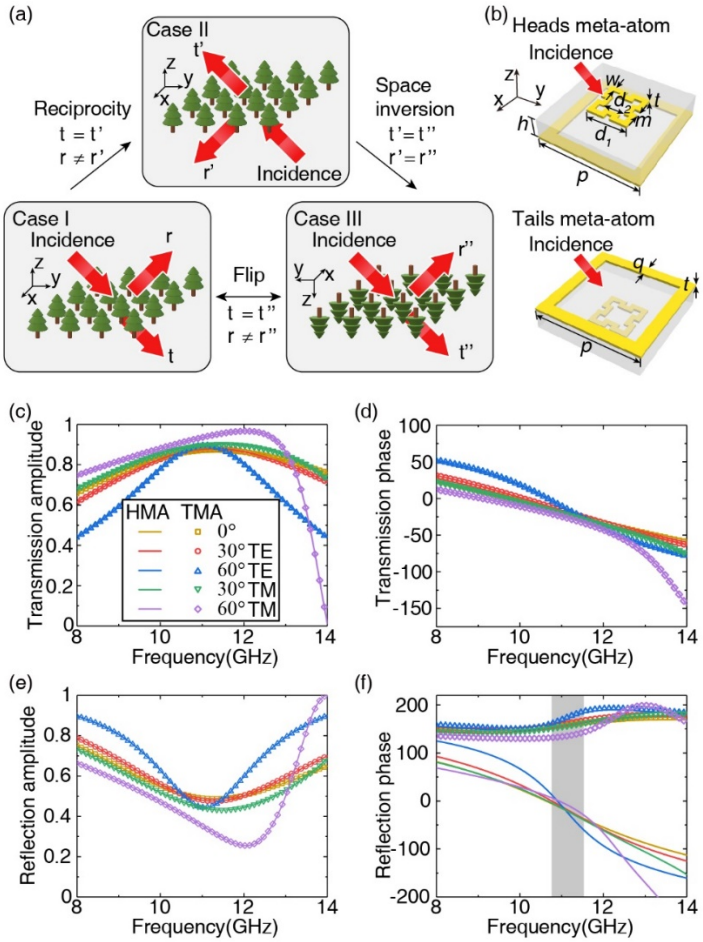

Fig. 2. The design of meta-atoms with identical transmissions and distinguishing reflections. (a) The reciprocity principle and space-inversion invariance jointly guarantee the unchanged transmission under the flip operation for the same incidence while the reflections can be distinctly different. (b) The two types of meta-atoms are related to each other by the space-inversion (flip) operation. Each meta-atom is composed of two layers of metallic pattern separated by a dielectric spacer with a height of $h = 2mm$ and a relative permittivity of $\varepsilon_r = 2.65$. Other geometric parameters of the metallic pattern are $p = 10.2mm$, $t = 0.036mm$, $w = 0.5mm$, $m = 0.5mm$, $d_1 = 4mm$, $d_2 = 2mm$ and $q = 1.1mm$, respectively. (c-f) The calculated amplitude and phase in transmission and reflection of the two types of meta-atoms under TE and TM polarized incident beam at the incident angles of 0°, 30° and 60°, respectively. The solid lines represent heads meta-atom (HMA) and the symbols represent tails meta-atom (TMA).

Optics EXPRESS

3. Camouflaged meta-dome with diffuse reflection and undistorted transmission

Radome protects the radar from the damage stemming from the environment. Recently, metasurface-based radomes, also referred to as meta-domes, have been demonstrated to improve the scan range of the radar [44]. Here, we propose that a random-flip metasurface (RFM) constructed by arranging HMA and TMA randomly can function as a camouflaged meta-dome, as schematically shown in Fig. 3(a). Since the meta-dome does not change the wavefront of incident waves in a broad spectrum, the radar protected by the meta-dome (depicted by red color) can function normally. On the other hand, the random binary reflection phase produces diffuse reflection that significantly reduces the signature of the reflection from the dome structure, making the meta-dome more difficult to be detected by other radar (depicted by blue color).

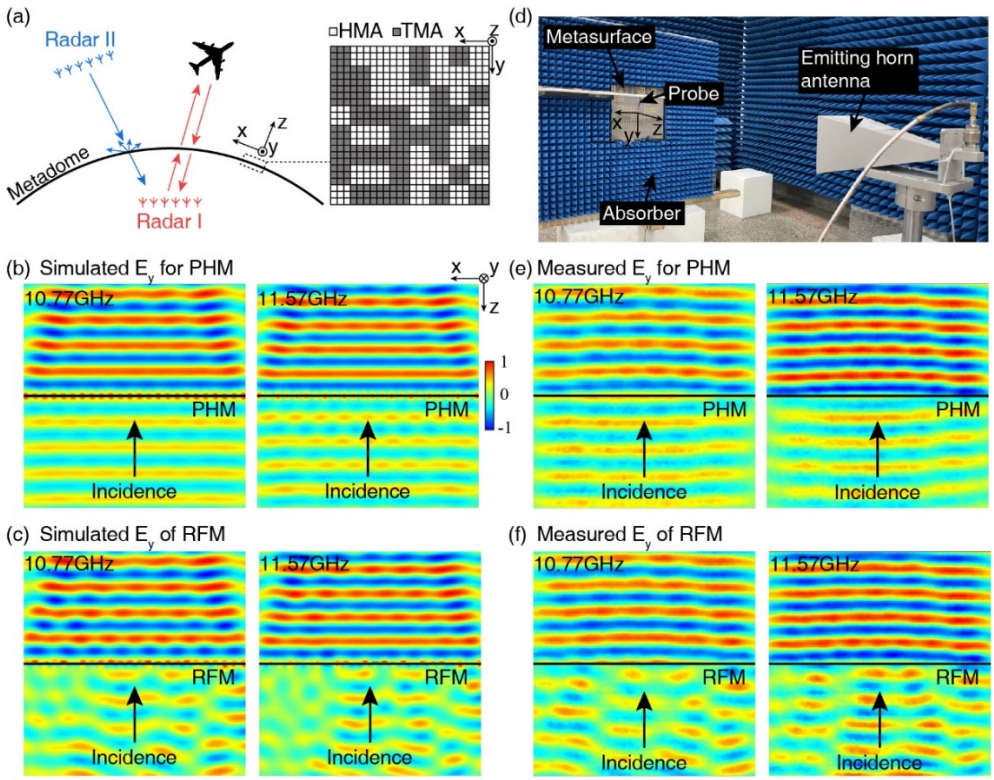

Fig. 3. The design of RFMs and camouflaged meta-domes. (a) Schematic of the camouflaged meta-dome based on a RFM (left panel) and the optimized distribution of the two types of meta-atoms (right panel). (b,c) The simulated electric-field distributions of scattered waves for a PHM (b) and a RFM (c) under the TE-polarized normal incident beam at 10.77 GHz and 11.57 GHz. (d) Experimental setup for near-field measurements. (e,f) The measured electric-field distributions of the scattered waves for a PHM (e) and a RFM (f) under the TE-polarized normal incident beam at 10.77 GHz and 11.57 GHz

Without loss of generality, here we design a random-flip metasurface that functions as a camouflaged meta-dome by using the meta-atoms in Fig. 2(b). A supercell of square 3×3 HMA or TMA is utilized as the metasurface block and referred to as the heads block or tails block, respectively. The random-flip metasurface is composed of 8×8 metasurface blocks, i.e., 24×24 meta-atoms. The random pattern of the heads and tails block shown in Fig. 3(a) is optimized by using the artificial bee colony algorithm, where the peak value of the scattering far-field is

Optics EXPRESS

employed as the fitness value (see more details in Supplement 1). The scattered field distributions of the designed RFM are simulated by full-wave simulations under the illumination of a normally incident Gaussian beam. For comparison, a pure-head metasurface (PHM) composed of only HMA is also investigated. Figure 3(b) shows the scattered electric fields of the PHM under a TE-polarized incidence with the electric field along the z-direction at 10.77 GHz and 11.57 GHz. It is seen that both the transmitted wave in –z half-space and the reflected wave in + z half-space possess a plane wavefront. The scattered electric fields of the RFM under the same incidence are illustrated in Fig. 3(c), which shows that the transmitted wave is the same as the plane wave, just like the case of PHM. While the wavefront of the reflected wave is disordered, in sharp contrast to the case of PHM.

This phenomenon is also verified by microwave experiments. The RFM and PHM are fabricated by printed circuit board technology. The experimental setup is shown in Fig. 3(d). An emitting horn antenna 1.5 m away from the metasurface is used to generate a quasi-plane-wave incident beam. The electric field is measured by a probing antenna mounted on a stepper motor. The emitting horn antenna and the probing antenna are connected to a KEYSIGHT N5224B network analyzer to acquire both the magnitude and phase of the microwave signal at the position of the probing antenna. Considering that the width of the incident beam is broader than that of the metasurface, microwave absorbers are placed surrounding the metasurface to prevent waves from bypassing the metasurface. The measured scattered electric fields of the PHM and RFM at 10.77 GHz and 11.57 GHz in the $y = 0$ plane are, respectively, shown in Figs. 3(e) and 3(f). The measured results are in good agreement with the simulation results, and this confirms that the RFM simultaneously realizes diffuse reflection and undistorted transmission.

This phenomenon actually applies to a wide range of incident angles. Figures 4(a) and 4(b) show, respectively, the simulated scattered electric fields of the PHM and RFM under a TE-polarized beam at the incident angle of 30°. It is seen that PHM produces undistorted transmission and specular reflection with an undistorted plane wavefront. Contrarily, in the case of RFM, the specular reflection changes into diffuse reflection as manifested by the disordered wavefront of the scattered waves. The measured scattered electric fields of the PHM and RFM under a TE-polarized beam at the incident angle of 30° are shown in Figs. 4(c) and 4(d), respectively. The measured results are coincident with the simulation results, verifying the diffuse reflection and undistorted transmission of the RFM under oblique incidence.

We also investigated the far-field radiation pattern of the metasurface under the incidence with different incident angles, frequencies, and polarizations. Figure 5(a) shows the far-field radiation patterns of the PHM (left panel) and RFM (right panel) obtained by full-wave simulations under TE-polarized normal incident beam from the z-direction at 11.16 GHz. In both cases, a strong radiation lobe corresponding to the transmission appears in the same direction of the incidence, indicating that the random configuration of the RFM has almost no influence on the transmission. In the reflection, a large radiation lobe corresponding to the specular reflection occurs for the PHM. However, many small lobes in different directions are observed in the reflection from the RFM, indicating that the reflection is redistributed in various directions. The maximum intensity of the radiation for all directions is much weaker than that of the specular reflection, which is the hallmark of diffuse reflection. Figure 5(c) shows the simulated far-field radiation patterns of the PHM (solid lines) and RFM (dashed lines) under TE-polarized incident beam with the incident angles of $\theta_i = 10°$ and $\theta_i = 30°$ at 10.57 GHz and 11.77 GHz in the $y = 0$ plane. From Fig. 5(c), it is seen that the transmission lobes of the RFM and the PHM are almost identical and appear in the direction of incidence. While the specular reflection lobes, as seen in the case of PHM, changes into many small lobes in the case of RFM. Specifically, the intensity of the specular reflection in the case of RFM is reduced by 11.69 dB and 10.55 dB by comparison with that in the case of PHM for the incident angles of $\theta_i = 10°$ and $\theta_i = 30°$ at 10.77 GHz, respectively. At 11.57 GHz, such reductions are further reduced to 14.28 dB and 14.32 dB, respectively.

Optics EXPRESS

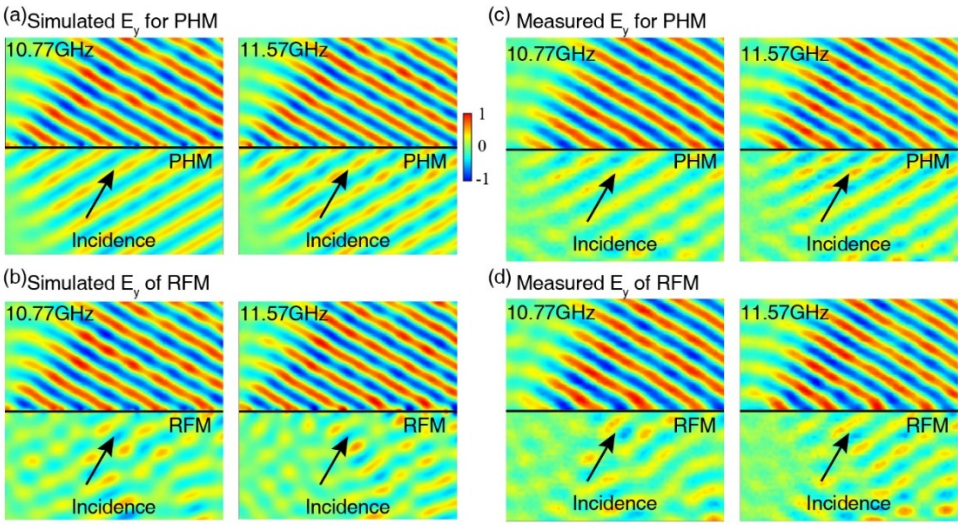

Fig. 4. RFM under oblique incidence. (a,b) The simulated scattered electric field of a PHM (a) and a RFM (b) under a TE-polarized beam at an incident angle of $\theta_i = 30°$ at 10.77 GHz and 11.57 GHz. (c,d) The measured scattered electric field of a PHM (c) and a RFM (d) under a TE-polarized incident beam at an incident angle of $\theta_i = 30°$ at 10.77 GHz and 11.57 GHz.

The far-field radiation patterns of the metasurface are also measured in microwave experiments. The experimental setup is shown in Fig. 5(b). A receiving horn antenna, which can rotate around the metasurface along a circular track, is used to measure the far-field radiation pattern at each polar angle θ in the x-z plane. We measured the far-field radiation patterns at the incident angles of $\theta_i = 10°$ and $\theta_i = 30°$. The measured radiation patterns of the PHM and RFM under a TE- polarized incident beam at 10.77 GHz and 11.57 GHz are shown in Fig. 5(d). Clearly, the measured results agree qualitatively with the simulation results in Fig. 5(c). Specifically, the intensity of the specular reflection in the case of RFM is measured to be reduced by 12.01 dB and 16.02 dB by comparison with that in the case of PHM for incidence with $\theta_i = 10°$ and $\theta_i = 30°$ at 10.77 GHz, respectively. At 11.57 GHz, they are reduced by 11.61 dB and 6.38 dB, respectively. The fluctuation in performance is probably induced by the fabrication error of the metasurfaces.

Optics EXPRESS

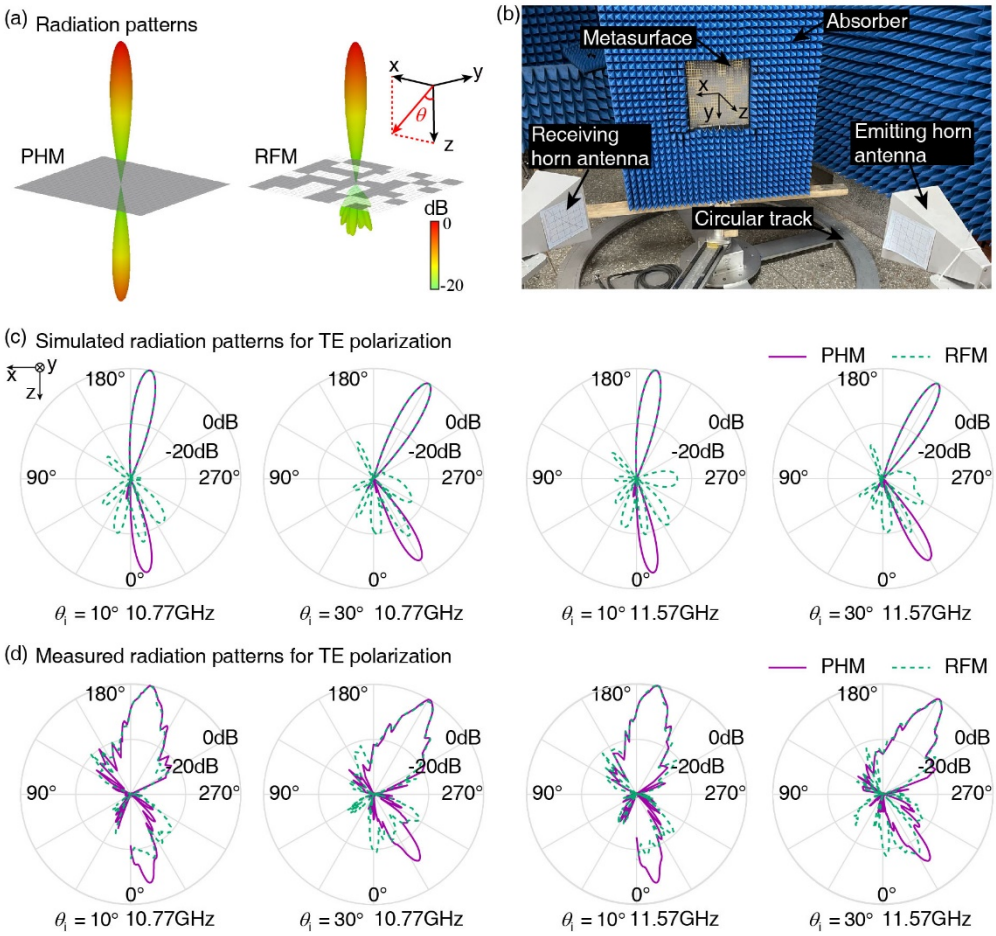

Fig. 5. Far-field radiation patterns of the RFM under a TE-polarized incident beam. (a) Far-field radiation patterns of a PHM (left panel) and a RFM (right panel) under a TE-polarized normal incident beam. (b) Experimental setup for the far-field radiation measurements. (c,d) The simulated (c) and measured (d) far-field radiation patterns of a PHM (solid lines) and a RFM (dashed lines) under incident beam at incident angles of $\theta_i = 10^\circ$ and $\theta_i = 30^\circ$ at 10.77 GHz and 11.57 GHz.

Optics EXPRESS

4. Discussion and conclusion

We note that in order to independently control the transmission and reflection, the phase correlation between reflection and transmission has to be broken and a lot of efforts have been devoted to achieving this goal. One approach is to employ two channels with orthogonal polarizations, but the functionality relies heavily on the polarization [45–48]. Another approach is to mix a series of total-reflection and total-transmission meta-atoms adjacently, but the tradeoff is the sacrifice of the spatial resolution [49,50]. Here, due to the C4v symmetry of the HMA and TMA, the functionality of the meta-dome applies to both TE and TM polarizations (demonstrated and shown in Supplement 1). Moreover, the optimal working bandwidth of manipulated reflection from this meta-dome is roughly from 10.77 GHz to 11.57 GHz. While the bandwidth of ordinary transmission through this meta-dome is very large, e.g. below 29.39 GHz, where the wavelength is smaller than the lattice constant of the meta-atoms, i.e., $p = 10.2mm$ and hence the grating effect is suppressed. Therefore, our approach has the significant advantages of broad bandwidth and insensitivity to the incident angle as well as the polarization. These remarkable features attribute to the utilization of reciprocity and spatial-inversion symmetry in the design of the metasurface.

It is important to note that although the previously demonstrated meta-domes are planar, our theory also applies to meta-domes with small curvatures. An example of curved meta-domes is shown in Supplement 1, where diffuse reflection is also realized, although the radiation patterns are a little different from those of the planar one. Here, we focus on planar geometries or small curvatures because they lead to the strong specular reflection that needs to be dealt with in practice.

We also note that the manipulated reflection is not limited to the diffuse reflection shown here. In fact, a range of functionalities, including focusing, beam splitting, and orbital-angular-momentum beam generation can be realized in reflection, without influencing the ordinary transmission. Due to the universality of the reciprocity principle and space-inversion symmetry, the functionality of flip-component metasurface is also irrespective of the absorption and resonance. By using similar principles, the coexistence of manipulated reflection and ordinary transmission can be extended to other classical wave systems such as acoustic and elastic waves.

In summary, we introduced here the concept of flip-component metasurface that combines manipulated reflection and ordinary transmission. This metasurface is composed of a pair of meta-atoms, which are the flip counterparts to each other. The reciprocity principle and space-inversion symmetry protect the identical transmission of the two types of meta-atoms, while their reflection phases are distinctly different. By arranging the two types of meta-atoms properly, the reflection can be manipulated. Meanwhile, the identical transmission guarantees undistorted ordinary transmission that is immune to the arrangement of meta-atoms. Such a remarkable feature enables the camouflaged meta-dome in the microwave frequency regime, which is hereby demonstrated both numerically and experimentally.

Funding. National Key Research and Development Program of China (2020YFA0211300, 2017YFA0303702); National Natural Science Foundation of China (11634005, 11974176, 11974177, 12174188, 61975078).

Disclosures. The authors declare no conflicts of interest.

Data availability. Data underlying the results presented in this paper are not publicly available at this time but may be obtained from the authors upon reasonable request.

Supplemental document. See Supplement 1 for supporting content.

References

1. N. I. Zheludev and Y. S. Kivshar, "From metamaterials to metadevices," Nat. Mater. **11**(11), 917–924 (2012).
2. H. Chen, C. T. Chan, and P. Sheng, "Transformation optics and metamaterials," Nat. Mater. **9**(5), 387–396 (2010).
3. S. Sun, Q. He, J. Hao, S. Xiao, and L. Zhou, "Electromagnetic metasurfaces: physics and applications," Adv. Opt. Photonics **11**(2), 380 (2019).
4. N. Yu and F. Capasso, "Flat optics with designer metasurfaces," Nat. Mater. **13**(2), 139–150 (2014).

Optics EXPRESS

5. N. Yu, P. Genevet, M. A. Kats, F. Aieta, J. P. Tetienne, F. Capasso, and Z. Gaburro, "Light Propagation with Phase Discontinuities: Generalized Laws of Reflection and Refraction," Science **334**(6054), 333–337 (2011).
6. X. Ni, N. K. Emani, A. V. Kildishev, A. Boltasseva, and V. M. Shalaev, "Broadband Light Bending with Plasmonic Nanoantennas," Science **335**(6067), 427 (2012).
7. F. Aieta, P. Genevet, N. Yu, M. A. Kats, Z. Gaburro, and F. Capasso, "Out-of-Plane Reflection and Refraction of Light by Anisotropic Optical Antenna Metasurfaces with Phase Discontinuities," Nano Lett. **12**(3), 1702–1706 (2012).
8. Y. Fu, C. Shen, Y. Cao, L. Gao, H. Chen, C. T. Chan, S. A. Cummer, and Y. Xu, "Reversal of transmission and reflection based on acoustic metagratings with integer parity design," Nat. Commun. **10**(1), 2326 (2019).
9. M. Khorasaninejad and F. Capasso, "Metalenses: Versatile multifunctional photonic components," Science **358**(6367), m8100 (2017).
10. W. T. Chen, A. Y. Zhu, V. Sanjeev, M. Khorasaninejad, Z. Shi, E. Lee, and F. Capasso, "A broadband achromatic metalens for focusing and imaging in the visible," Nat. Nanotechnol. **13**(3), 220–226 (2018).
11. S. Wang, P. C. Wu, V. Su, Y. Lai, M. Chen, H. Y. Kuo, B. H. Chen, Y. H. Chen, T. Huang, J. Wang, R. Lin, C. Kuan, T. Li, Z. Wang, S. Zhu, and D. P. Tsai, "A broadband achromatic metalens in the visible," Nat. Nanotechnol. **13**(3), 227–232 (2018).
12. M. Khorasaninejad, W. T. Chen, R. C. Devlin, J. Oh, A. Y. Zhu, and F. Capasso, "Metalenses at visible wavelengths: Diffraction-limited focusing and subwavelength resolution imaging," Science **352**(6290), 1190–1194 (2016).
13. S. Sun, Q. He, S. Xiao, Q. Xu, X. Li, and L. Zhou, "Gradient-index meta-surfaces as a bridge linking propagating waves and surface waves," Nat. Mater. **11**(5), 426–431 (2012).
14. W. Sun, Q. He, S. Sun, and L. Zhou, "High-efficiency surface plasmon meta-couplers: concept and microwave-regime realizations," Light: Sci. Appl. **5**(1), e16003 (2016).
15. H. C. Chu, J. Luo, and Y. Lai, "Efficient way to convert propagating waves into guided waves via gradient wire structures," Opt. Lett. **41**(15), 3551–3554 (2016).
16. H. Chu, J. Luo, and Y. Lai, "A Metacoupler for Converting Propagating Waves to Guided Waves in Wire Waveguides," Ieee Photonics J. **9**(5), 1–7 (2017).
17. Z. Wang, S. Li, X. Zhang, X. Feng, Q. Wang, J. Han, Q. He, W. Zhang, S. Sun, and L. Zhou, "Excite Spoof Surface Plasmons with Tailored Wavefronts Using High-Efficiency Terahertz Metasurfaces," Adv. Sci. **7**(19), 2000982 (2020).
18. L. Huang, S. Zhang, and T. Zentgraf, "Metasurface holography: from fundamentals to applications," Nanophotonics **7**(6), 1169–1190 (2018).
19. G. Zheng, H. Mühlenbernd, M. Kenney, G. Li, T. Zentgraf, and S. Zhang, "Metasurface holograms reaching 80% efficiency," Nat. Nanotechnol. **10**(4), 308–312 (2015).
20. B. Xiong, Y. Xu, J. Wang, L. Li, L. Deng, F. Cheng, R. W. Peng, M. Wang, and Y. Liu, "Realizing Colorful Holographic Mimicry by Metasurfaces," Adv. Mater. **33**(21), 2005864 (2021).
21. Z. L. Deng, M. Jin, X. Ye, S. Wang, T. Shi, J. Deng, N. Mao, Y. Cao, B. O. Guan, A. Alù, G. Li, and X. Li, "Full-Color Complex-Amplitude Vectorial Holograms Based on Multi-Freedom Metasurfaces," Adv. Funct. Mater. **30**(21), 1910610 (2020).
22. X. Ni, Z. J. Wong, M. Mrejen, Y. Wang, and X. Zhang, "An ultrathin invisibility skin cloak for visible light," Science **349**(6254), 1310–1314 (2015).
23. J. Zhang, Z. L. Mei, W. R. Zhang, F. Yang, and T. J. Cui, "An ultrathin directional carpet cloak based on generalized Snell's law," Appl. Phys. Lett. **103**(15), 151115 (2013).
24. Y. Yang, L. Jing, B. Zheng, R. Hao, W. Yin, E. Li, C. M. Soukoulis, and H. Chen, "Full-Polarization 3D Metasurface Cloak with Preserved Amplitude and Phase," Adv. Mater. **28**(32), 6866–6871 (2016).
25. H. Chu, Q. Li, B. Liu, J. Luo, S. Sun, Z. H. Hang, L. Zhou, and Y. Lai, "A hybrid invisibility cloak based on integration of transparent metasurfaces and zero-index materials," Light: Sci. Appl. **7**(50), 1–8 (2018).
26. H. Chu, H. Zhang, Y. Zhang, R. Peng, M. Wang, Y. Hao, and Y. Lai, "Invisible surfaces enabled by the coalescence of anti-reflection and wavefront controllability in ultrathin metasurfaces," Nat. Commun. **12**(1), 4523 (2021).
27. C. Wang, Z. Zhu, W. Cui, Y. Yang, L. Ran, and D. Ye, "All-angle Brewster effect observed on a terahertz metasurface," Appl. Phys. Lett. **114**(19), 191902 (2019).
28. J. Luo, H. Chu, R. Peng, M. Wang, J. Li, and Y. Lai, "Ultra-broadband reflectionless Brewster absorber protected by reciprocity," Light-Sci. Appl. **10**(1), 89 (2021).
29. G. Lavigne and C. Caloz, "Generalized Brewster effect using bianisotropic metasurfaces," Opt. Express **29**(7), 11361 (2021).
30. A. Forbes, M. de Oliveira, and M. R. Dennis, "Structured light," Nat. Photonics **15**(4), 253–262 (2021).
31. H. Larocque, D. Sugic, D. Mortimer, A. J. Taylor, R. Fickler, R. W. Boyd, M. R. Dennis, and E. Karimi, "Reconstructing the topology of optical polarization knots," Nat. Phys. **14**(11), 1079–1082 (2018).
32. L. Wang, W. Zhang, H. Yin, and X. Zhang, "Ultrasmall Optical Vortex Knots Generated by Spin-Selective Metasurface Holograms," Adv. Opt. Mater. **7**(10), 1900263 (2019).
33. N. K. Grady, J. E. Heyes, D. R. Chowdhury, Y. Zeng, M. T. Reiten, A. K. Azad, A. J. Taylor, D. A. R. Dalvit, and H. T. Chen, "Terahertz Metamaterials for Linear Polarization Conversion and Anomalous Refraction," Science **340**(6138), 1304–1307 (2013).
34. R. Fan, Y. Zhou, X. Ren, R. Peng, S. Jiang, D. Xu, X. Xiong, X. Huang, and W. Mu, "Freely Tunable Broadband Polarization Rotator for Terahertz Waves," Adv. Mater. **27**(7), 1201–1206 (2015).

Optics EXPRESS

35. Y. Gao, X. Xiong, Z. Wang, F. Chen, R. Peng, and M. Wang, "Simultaneous Generation of Arbitrary Assembly of Polarization States with Geometrical-Scaling-Induced Phase Modulation," Phys. Rev. X **10**(3), 31035 (2020).
36. A. H. Dorrah, N. A. Rubin, A. Zaidi, M. Tamagnone, and F. Capasso, "Metasurface optics for on-demand polarization transformations along the optical path," Nat. Photonics **15**(4), 287–296 (2021).
37. Q. Hu, K. Chen, N. Zhang, J. Zhao, T. Jiang, J. Zhao, and Y. Feng, "Arbitrary and Dynamic Poincaré Sphere Polarization Converter with a Time-Varying Metasurface," Adv. Opt. Mater. **1**, 2101915 (2021).
38. X. Chen, L. Huang, H. Mühlenbernd, G. Li, B. Bai, Q. Tan, G. Jin, C. Qiu, S. Zhang, and T. Zentgraf, "Dual-polarity plasmonic metalens for visible light," Nat. Commun. **3**(1), 1198 (2012).
39. W. Luo, S. Sun, H. Xu, Q. He, and L. Zhou, "Transmissive Ultrathin Pancharatnam-Berry Metasurfaces with nearly 100% Efficiency," Phys. Rev. Appl. **7**(4), 044033 (2017).
40. M. R. Akram, G. Ding, K. Chen, Y. Feng, and W. Zhu, "Ultrathin Single Layer Metasurfaces with Ultra-Wideband Operation for Both Transmission and Reflection," Adv. Mater. **32**(12), 1907308 (2020).
41. A. C. Overvig, S. C. Malek, and N. Yu, "Multifunctional Nonlocal Metasurfaces," Phys. Rev. Lett. **125**(1), 017402 (2020).
42. D. Lin, P. Fan, E. Hasman, and M. L. Brongersma, "Dielectric gradient metasurface optical elements," Science **345**(6194), 298–302 (2014).
43. H. Chu, X. Xiong, Y. Gao, J. Luo, H. Jing, C. Li, R. Peng, M. Wang, and Y. Lai, "Diffuse reflection and reciprocity-protected transmission via a random-flip metasurface," Sci. Adv. **7**(37), j935 (2021).
44. A. Benini, E. Martini, S. Monni, M. C. Vigano, F. Silvestri, E. Gandini, G. Gerini, G. Toso, and S. Maci, "Phase-Gradient Meta-Dome for Increasing Grating-Lobe-Free Scan Range in Phased Arrays," IEEE Trans. Antennas Propagat. **66**(8), 3973–3982 (2018).
45. L. Zhang, R. Y. Wu, G. D. Bai, H. T. Wu, Q. Ma, X. Q. Chen, and T. J. Cui, "Transmission-Reflection-Integrated Multifunctional Coding Metasurface for Full-Space Controls of Electromagnetic Waves," Adv. Funct. Mater. **28**(33), 1802205 (2018).
46. Y. Zhuang, G. Wang, T. Cai, and Q. Zhang, "Design of bifunctional metasurface based on independent control of transmission and reflection," Opt. Express **26**(3), 3594 (2018).
47. X. Zhang, M. Pu, Y. Guo, J. Jin, X. Li, X. Ma, J. Luo, C. Wang, and X. Luo, "Colorful Metahologram with Independently Controlled Images in Transmission and Reflection Spaces," Adv. Funct. Mater. **29**(22), 1809145 (2019).
48. T. Cai, G. M. Wang, S. W. Tang, H. X. Xu, J. W. Duan, H. J. Guo, F. X. Guan, S. L. Sun, Q. He, and L. Zhou, "High-Efficiency and Full-Space Manipulation of Electromagnetic Wave Fronts with Metasurfaces," Phys. Rev. Appl. **8**(3), 034033 (2017).
49. K. Chen, G. Ding, G. Hu, Z. Jin, J. Zhao, Y. Feng, T. Jiang, A. Alù, and C. W. Qiu, "Directional Janus Metasurface," Adv. Mater. **32**(2), 1906352 (2020).
50. Y. Wang, Y. Ge, Z. Chen, X. Liu, J. Pu, K. Liu, H. Chen, and Y. Hao, "Broadband High-Efficiency Ultrathin Metasurfaces With Simultaneous Independent Control of Transmission and Reflection Amplitudes and Phases," IEEE Trans. Microwave Theory Techn. **70**(1), 254–263 (2022).